IEEE Access
Multidisciplinary | Rapid Review | Open Access Journal

Received January 5, 2019, accepted January 22, 2019, date of publication January 30, 2019, date of current version February 20, 2019.

Digital Object Identifier 10.1109/ACCESS.2019.2896148

Star Detection and Accurate Centroiding for the Geosynchronous Interferometric Infrared Sounder of Fengyun-4A

HAOPENG ZHANG[1,2,3], (Member, IEEE), YI SU[1,2,3], LEI YANG[4], JIAN SHANG[4], CHENGBAO LIU[4], JING WANG[4], SHENGXIONG ZHOU[5], ZHIGUO JIANG[1,2,3], (Member, IEEE), AND ZHIQING ZHANG[4]

[1]Image Processing Center, School of Astronautics, Beihang University, Beijing 100191, China
[2]Key Laboratory of Spacecraft Design Optimization and Dynamic Simulation Technologies, Ministry of Education, Beijing 100191, China
[3]Beijing Key Laboratory of Digital Media, Beijing 100191, China
[4]National Satellite Meteorological Center, China Meteorological Administration, Beijing 100081, China
[5]Southwest Electronics and Telecommunication Technology Research Institute, Chengdu 610000, Sichuan, China

Corresponding authors: Lei Yang (yangl@cma.gov.cn), Jian Shang (shangjian@cma.gov.cn), Zhiguo Jiang (jiangzg@buaa.edu.cn), and Zhiqing Zhang (zqzhang@cma.gov.cn)

This work was supported in part by the National Natural Science Foundation of China under Grant 61501009, Grant 61771031, Grant 91338109, and Grant 61172113, in part by the National Key Research and Development Program of China under Grant 2016YFB0501300 and Grant 2016YFB0501302, and in part by the Fundamental Research Funds for the Central Universities.

ABSTRACT Extracting accurate star centroids in the observed star images is one of the key problems for image navigation of the geosynchronous interferometric infrared sounder (GIIRS) of Fengyun-4A Satellite (FY-4A), the first scientific experimental satellite of the new generation of Chinese geostationary meteorological satellite Fengyun-4 series. Compared with star sensors which are widely used for star observation, it is challenging to detect the 2×2 star spot from the focused star images of GIIRS and calculate the star centroid in high precision. In this paper, we propose a star detection and centroiding method based on trajectory search and trajectory fitting. Since the launch of FY-4A in December 2016, our centroiding method has been tested in-orbit for over two years. The extensive experiments show that the star centroiding error of our method is less than 0.3 pixels, which makes an important contribution to image navigation of FY-4A.

INDEX TERMS Star centroiding, trajectory fitting, star recognition, Fengyun-4A, geostationary satellite.

I. INTRODUCTION

Fengyun-4 (FY-4) is the new generation of geostationary meteorological satellite developed by China [1]–[3]. The first satellite of FY-4 series, Fengyun-4A (FY-4A), was launched on December 11, 2016 as a scientific experimental satellite. Compared with the first generation spin-stabilized geostationary satellites Fengyun-2 (FY-2), FY-4 employs the three-axis stabilized platform, declining the period of every full-disc coverage from 30 to 15 minutes (even fewer) as well as realizing flexible regional observation. Four new instruments are aboard FY-4A [1], [4] to generate remote sensing products, including Advanced Geosynchronous Radiation Imager (AGRI), the Geosynchronous Interferometric Infrared Sounder (GIIRS), the Lightning Mapping Imager (LMI), and the Space Environment Package (SEP).

Image navigation is a key problem for meteorological satellite, since it makes a direct influence on the quality of remote sensing products [5]. Different from the image navigation technology of FY-2 based on the observation of landmarks, an advanced technology based on star sensing is applied to FY-4A. By contrast, the latter directly acquires the point of the instrument without the restrictions of cloud and observable period, and most importantly, with higher precision [6]. Thus star centroid detection is one of the key technologies for image navigation of FY-4A.

Star centroid detection is usually used on star sensors for celestial navigation, and many researches have been made in this field [7]–[9]. Different from the star sensors which are specially designed for star scan, as one of the major instruments of FY-4A, GIIRS is a focal detector mainly used

The associate editor coordinating the review of this manuscript and approving it for publication was Vincenzo Piuri.

TABLE 1. Primary performance indicator and navigation precision of GIIRS aboard FY-4A.

Indicators	Parameters	
Spectral parameters	long wave: short/medium wave: visible light:	700-1130 cm^{-1} 1650-2250 cm^{-1} 0.55-0.75 μm
Spectral resolution (cm^{-1})	small and middle scale: region detection:	long wave 0.8; medium wave 1.6 long wave 1.6; medium wave 3.2
Sensitivity and SNR	small and middle scale: region (stride): visible light:	long wave 0.5-1.1; medium wave 0.1-0.14 long wave 0.5-1.1; medium wave 0.1-0.14 S/N$\geq$200 ($\rho = 100\%$)
Spatial resolution	sub-satellite point:	16 km(infrared); 2 km(visible)
Temporal resolution	small and medium scale: region:	35 minutes 67 minutes
Detection area	small and medium scale: region:	1000 km$\times$1000 km 5000 km$\times$5000 km
Navigation precision		1 IR pixel

for atmosphere observation [1], [10]. The energy of the star spot on GIIRS is focused on a region smaller than 3 $\times$ 3 pixels (2 $\times$ 2 in general). As a result, the star spot resembles the noisy pixels a lot. Furthermore, compared with the high imaging frequency 500 Hz of AGRI [11] of FY-4A, the imaging frequency of GIIRS is one hundredfold lower. Thus, less data can be generated by GIIRS for star centroiding, and the method based on energy response curve fitting for AGRI [11] is no longer valid for GIIRS. In addition, GIIRS has a wider instantaneous field of view (IFOV) than AGRI, making it possible that more than one star will be captured. Therefore, the predicted star to be sensed for image navigation should be distinguished from others before star centroiding. Overall, these characteristics make it a challenge to detect stars and calculate their centroids in high precision for GIIRS.

Aiming to solve the problems, this paper proposes a star detection and centroiding method for GIIRS aboard FY-4A. Firstly, the fixed noise of the star images caused by the reflection of the atmosphere is removed to improve signal-noise ratio. Secondly, the images of a star sensing are fused into a single image with star trajectory, in order to convert the hard problem of weak point detection to an easier problem of line detection. Then, according to the information of star catalog, we use triangular and angular distance recognition method to find out the predicted star for image navigation. Finally, the sub-pixel centroid of the predicted star is calculated based on trajectory fitting as [11]. Experimental results on simulated star images in various conditions and real star sensing images of in-orbit testing of FY-4A validate the feasibility and effectiveness of our method for robust star detection and accurate centroiding of GIIRS aboard FY-4A.

The organization of the rest of this paper is as follows. Section II presents the essential properties of GIIRS conducting star sensing and gives an overview of our method. Section III introduces our method in detail, including preprocessing, star detection and recognition, and centroid extraction. The results of the simulated and in-orbit experiments are shown in Section IV and Section V respectively. Finally, Section VI is the conclusion of this paper.

II. OVERVIEW OF STAR SENSING IMAGE PROCESSING FOR GIIRS

A. PARAMETERS OF GIIRS

As the first high-spectral-resolution advanced infrared sounder installed on a geostationary weather satellite, GIIRS monitors the vertical temperature and moisture structure of the atmosphere continuously, playing an important role in the forecast of severe weather warning [1]. Table 1 shows the primary parameters of GIIRS.

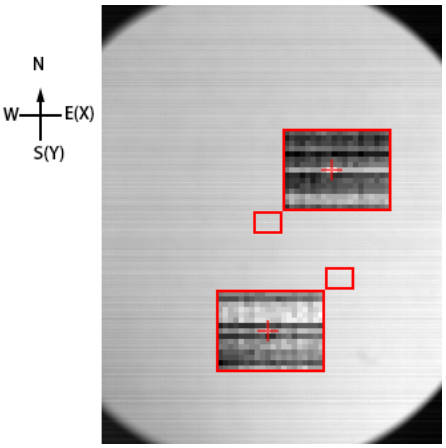

FIGURE 1. Star sensing result of GIIRS. Detected stars in the image are outlined in red bounding boxes with the centroids marked as red crosses in the magnified sub-views.

B. STAR SENSING OF GIIRS

The visible channel of GIIRS is used to scan the predicted star during the star sensing task between Earth observations. The scan angles of the two scan mirrors are calculated in advance, to rotate the line-of-sight (LOS) to the star. Due to the geostationary orbit of FY-4A, the star spot moves almost linearly in the image plane from the west to the east. Figure 1 shows an actual star image generated by GIIRS in orbit on July 25, 2017. The image plane of GIIRS consists of a detector with 330$\times$256 pixels, and the field of view for each pixel is 56 μrad. The corners of the star image are shaded by

the lens hood, which is used to reduce the influence of the stray light. The two star spots are outlined in red bounding boxes and the centroids are marked as red crosses in the magnified sub-views.

C. FLOWCHART OF STAR DETECTION AND CENTROIDING

The star sensing image processing for GIIRS aims to solve two problems. The one is to distinguish the unique spot of the predicted star from the image sequence in high accuracy, against the interference of the noise and the neighboring stars. The other is to calculate the sub-pixel centroid of the predicted star in high precision. A novel processing procedure is proposed to solve the two practical problems, shown in Figure 2. We firstly preprocess the star image with fixed noise removal to improve the quality of the image. Secondly, star detection is made based on the star trajectory in the integrated image of the whole sequence of star sensing images. Then, star recognition is employed with the triangle matching method. Finally, sub-pixel star centroid in high precision is extracted through the fitting of the trajectories in both X and Y directions. Details of the proposed method will be introduced in the following section.

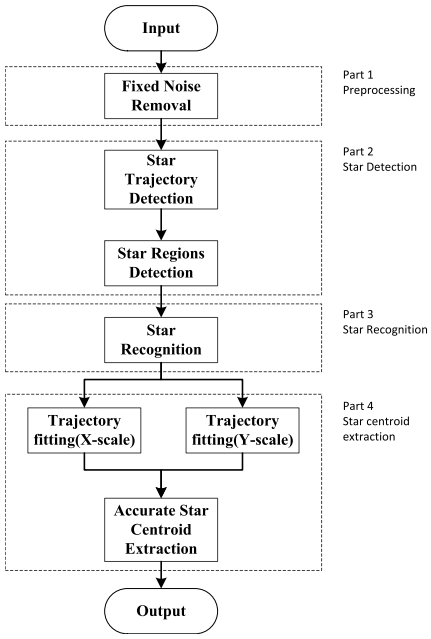

FIGURE 2. The flowchart of star detection and centroiding for GIIRS of FY-4A.

III. METHODS

A. IMAGE PREPROCESSING FOR GIIRS

Actual star images contain strong noise caused by the atmospheric reflection, since the field of view of GIIRS is close to the Earth disk. The image noise makes a direct impact on the signal-noise ratio and the contrast, causing a difficult situation for star detection and centroiding. According to the statistical character, the noise in the images can be sorted into the fixed noise and the random noise.

Fixed noise is the low-frequency component as

$$I^{noise}(x,y) = \frac{\sum_{k=1}^{C} I_k(x,y)}{C} \tag{1}$$

where C is the total frame number of the star image sequence, $I_k(x,y)$ is the gray value of the pixel (x,y) in the k-th image, and $I^{noise}(x,y)$ is the fixed noise mask.

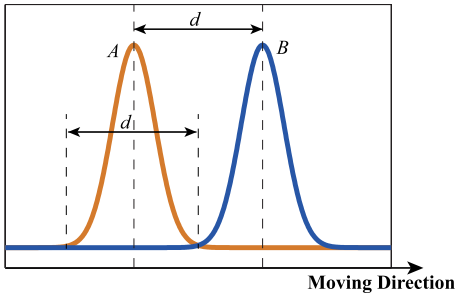

FIGURE 3. The star spot moves from the position *A* to position *B*. The star spots in two images are non-overlapping until the distance reaches *d*, i.e. the diameter of the star spot.

Equation 1 calculates a single mask, which is used to remove the fixed noise in the total sequence. However, this strategy results in the loss of the star energy. As shown in Figure 3, the star spot moves in a straight trajectory during star sensing. The vast majority energy of the star spot is distributed within a region of $d \times d$ pixels. Overlap does not exist if the distance of the two spots is greater than d. Thus, in practice, the images next to the target image $I_i(x,y)$ should not participate in the fixed noise calculation of $I_i(x,y)$.

Based on the geostationary orbit of FY-4A, the velocity of the star spot on the image can be calculated as

$$V_x = \frac{2\pi}{\zeta} \cdot \frac{1}{\psi} \cdot cos(\delta) \tag{2}$$

where $\zeta = 23\,h\,56\,min\,4\,sec$, $\psi = 56\,\mu rad$ is the angular resolution of a pixel, and δ is the declination of the line-of-sight (LOS) in Celestial Coordinate System (CCS).

In order to avoid affecting the energy of the star spots, a frame threshold N^s is used in the image preprocessing. That is to say the images in the N^s-neighbor of the i-th image do not participate in the calculation of the fixed noise mask. The number N^s between two non-overlapped frames is

$$N^s = d \cdot {V_x}^{-1} \cdot f \tag{3}$$

where $f = 3$ Hz is the frame frequency of GIIRS, and the pixel size of the star spot is $d \times d$ (2×2 for GIIRS). We set $N^s = 5$ to ensure the spot without overlap. Therefore, the fixed noise of each star image can be calculated as

$$I_i^n(x,y) = \frac{\sum_{|k-i|>N^s} I_k(x,y)}{C_i} \tag{4}$$

where $I_k(x,y)$ is the k-th image of a sequence, $I_i^n(x,y)$ is the noise mask applied to the fixed noise removal for the i-th star image, and C_i is the number of the images participating in the noise calculation, meeting the constraint of N^s-neighbor.

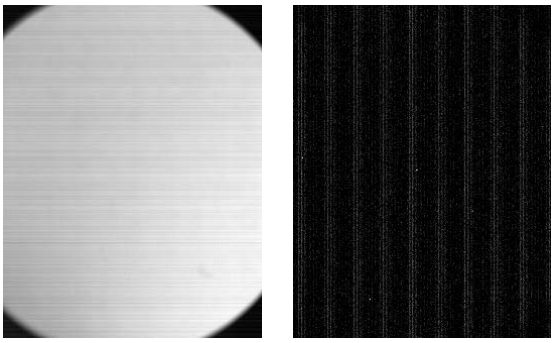

(**a**) (**b**)

FIGURE 4. (a) An original star image captured by GIIRS in-orbit on July 25, 2017. (b) The star image after fixed noise removal.

Given the fixed noise mask $I_i^n(x, y)$, the fixed noise removed image for the i-th star image can be obtained as

$$I_i^d(x, y) = \begin{cases} I_i(x, y) - I_i^n(x, y) & I_i^d(x, y) \geq 0 \\ 0 & I_i^d(x, y) < 0 \end{cases} \quad (5)$$

Figure 4 shows the images before and after fixed noise removal.

It should be noticed that after fixed noise removal, some pixels are still influenced by random noise, as shown in Figure 4 (**b**). It can be seen that the random noise has similar characteristic as stars. However, star image data available from GIIRS is insufficient because of its low frame frequency. As a result, not similar as AGRI aboard FY-4A, the energy response curve [11] of the detector where the star passes, cannot be fitted out or filtered to reduce random noise. In order to preserve the energy distribution of the star regions, which is important for high-precision centroid extraction, random noise filter is not used in our image preprocessing for GIIRS. The impact of the random noise will be solved in our detection and centroid extraction procedures.

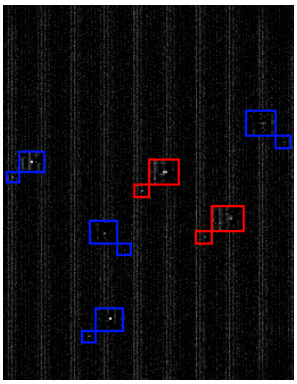

FIGURE 5. The two star spots in the image are marked in the red boxes, whereas some of the noise regions are in blue. Both of the two kinds of targets have the same characteristics in a single star image.

B. STAR DETECTION FOR GIIRS

As shown in Figure 5, due to the focal structure of GIIRS mentioned above, it is hard to find the visual difference between the star spot and the noisy pixels after fixed noise removal. Seeing that the sequence of star images contains the motion information of the stars, we can transform the task of still target detection in a single image to weak moving target detection in an image sequence. In view of the characteristics of GIIRS's star images, we propose a star trajectory detection method for GIIRS. Considering that the gray value of the star spot is usually higher than that of the other regions, a threshold segmentation method is used in advance to further reduce the noise in the preprocessed images, i.e.

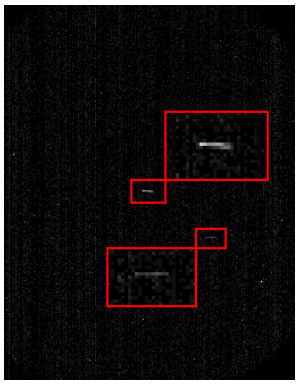

FIGURE 6. Star trajectory detection result in a fused star image.

$$I_i^{seg}(x, y) = \begin{cases} I_i^d(x, y) & I_i^d(x, y) \geq T_i^{seg} \\ 0 & I_i^d(x, y) < T_i^{seg} \end{cases} \quad (6)$$

where the threshold of the i-th star image T_i^{seg} can be

$$T_i^{seg} = mean(\mathbf{s}_i) + \alpha \cdot std(\mathbf{s}_i) \quad (7)$$

where $\mathbf{s}_i$ represents the non-zero pixels in the i-th image, α is an adjustment parameter, and $mean(\cdot)$ and $std(\cdot)$ stand for the mean value and standard deviation respectively. According to our experiment, we set $\alpha = 3$ to get good performance.

The values of most pixels in the segmented star images I^{seg} are zero, as a result of the fixed noise removal and threshold segmentation. The non-zero pixels are composed of the star spots and pixels with strong noise. To find the star trajectory, we fuse the multiple star images in the sequence of star sensing, and the fused image can be obtained as

$$I^{traj}(x, y) = \sum_{i=1}^{C} I_i^{seg}(x, y) \quad (8)$$

Based on the motion information of the satellite, the length ℓ of the star trajectory in image can be calculated as

$$\ell = V_x \cdot C \cdot f^{-1} \quad (9)$$

where the frame number C of the image sequence and the velocity V_x of the star spot are indicated in Equation 1 and 2. Then, the pixel regions of the star trajectories can be detected accurately by searching ℓ-pixel-long lines in the fusion image, as shown in Figure 6.

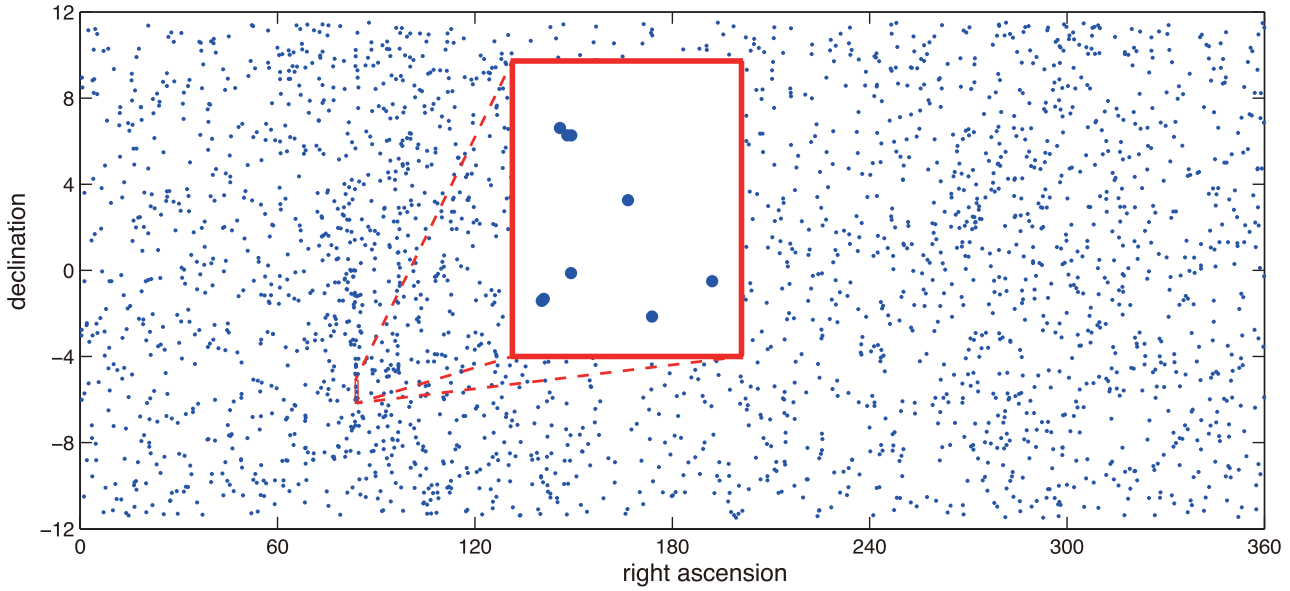

FIGURE 7. Star distribution map in the FOV of GIIRS. Each blue point stands for an observable star. A single region (with the directional angles of line-of-sight (LOS) $\alpha_{IFOV} = 84.063°$, $\delta_{IFOV} = -5.648°$) containing nine stars is shown as the red box.

C. STAR RECOGNITION FOR GIIRS

The size of the GIIRS star image is 330 × 256 pixels, covering an IFOV of around 1.06° × 0.82°. According to the star sensing mode of FY-4A, the FOV of GIIRS is in the equatorial band of the declination [−11.5°, 11.5°]. Figure 7 illustrates possible target stars which may appear in the FOV of GIIRS by analyzing the SAO star catalog. There are totally 2797 observable stars below magnitude 7.0, i.e. the sensitivity limit of GIIRS. The statistical result of these observable stars in the IFOV of GIIRS is shown in Table 2. We can see that more than one star could appear in the GIIRS star image, and the number of the stars appearing in the IFOV will be not greater than nine due to the small size of the IFOV. Thus star recognition is necessary to establish a correct mapping between the detected stars and the stars in the star catalog and then determine the unique target star, i.e. the predicted one to be sensed.

TABLE 2. The statistical result of the star number in the IFOV of GIIRS aboard FY-4A.

Star No.	1	2	3	4	5	6	7	8	9
IFOV No.	2730	1309	294	55	11	9	10	4	1

When at least three stars are sensed, the popular triangular algorithm [12], [13] can be used for star recognition, since it is able to construct certain amount of triangles in this case. In this method, image triangles and navigation triangles are constructed with the star spots in the image and the stars in star catalog respectively, as shown in Figure 8. The star angular distance is used as the main characteristic for star matching, with an advantage of small computation and rotation invariance.

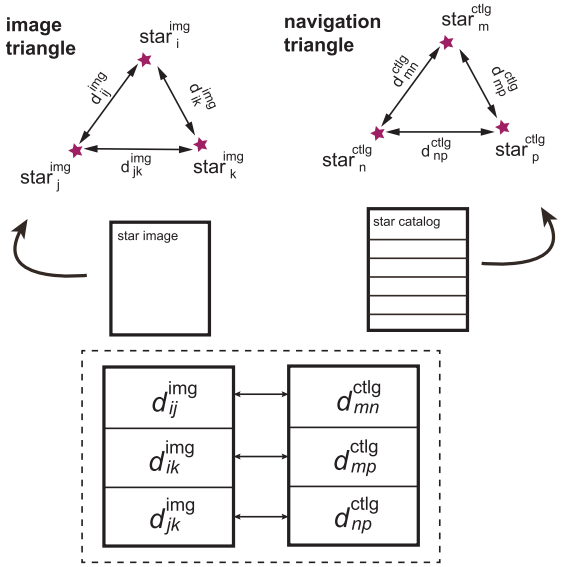

FIGURE 8. Star triangles for recognition. $star_i^{img}$ is the i-th star spot in the star image, and $star_m^{ctlg}$ is the m-th star in the catalog of the target region. d_{ij}^{img} is the angular distance between $star_i^{img}$ and $star_j^{img}$, and d_{mn}^{ctlg} is that between $star_m^{ctlg}$ and $star_n^{ctlg}$.

Particularly, the angular distances of the image triangles can be calculated as

$$d_{ij}^{img} = \psi \cdot \sqrt{(x_i - x_j)^2 + (y_i - y_j)^2} \tag{10}$$

where (x_i, y_i) and (x_j, y_j) are the coordinates of the i-th and j-th star spots, and ψ is the angular resolution of GIIRS. The angular distances of the navigation triangles can be

calculated as

$$d_{mn}^{ctlg} = arccos(sin(\delta_m) \cdot sin(\delta_n) + cos(\delta_m) \cdot cos(\delta_n) \cdot cos(\alpha_m - \alpha_n)) \quad (11)$$

where (α_m, δ_m) and (α_n, δ_n) are the right ascension and the declination of the m-th and the n-th stars.

In order to reduce the calculation in star matching, the three stars of a star triangle are sorted in a certain rule, i.e. energy (magnitude) or location. Compared with the energy of star spots which is more susceptible to noise, the coordinate is more reliable as the ordering rule. In our method, the stars are sorted by the Y coordinates (declinations for navigation triangles), making $y_i < y_j < y_k$ and $\delta_m > \delta_n > \delta_p$ (as shown in the lower sub-figure of Figure 8), where y_i is the y coordinate of the i-th star spot and δ_m is the declination of the m-th star in catalog. If the errors of the three corresponding pairs of angular distances in the image and navigation triangles are less than a matching threshold, the three star spots are matched to the three stars in catalog. In practice, the matching threshold is set to 0.00454°, which is corresponding to the field angle of $\sqrt{2}$ pixels.

As shown in Table 2, there will be less than three stars appearing in the IFOV of GIIRS in most cases. A star triangle is not able to be constructed when only two stars are detected in the star image, leading to invalidation of triangular algorithm. In this case, we match the detected angular distance in star image to those of the navigation triangles. The sorting process and the matching threshold are same with triangular method. When exactly one star is detected in the image, we regard the observed star as the predicted star. Considering the attitude stability of FY-4A and the pointing accuracy of GIIRS, such star recognition strategy for the cases of one or two stars can work well. This will be validated in our simulation experiments and practical in-orbit tests in Section IV and V respectively.

D. STAR CENTROID EXTRACTION

Center of Mass (COM) method [7] can be used to calculated the raw coordinates of the star centroid, according to the energy distribution of a star spot in a single frame, i.e.

$$\begin{cases} X_i = \dfrac{\sum_{(x,y)\in\Phi_i} x \cdot I_i(x,y)}{\sum_{(x,y)\in\Phi_i} I_i(x,y)} \\ Y_i = \dfrac{\sum_{(x,y)\in\Phi_i} y \cdot I_i(x,y)}{\sum_{(x,y)\in\Phi_i} I_i(x,y)} \end{cases} \quad (12)$$

where Φ_i is the star region of the i-th image, and set as 3×3 pixels based on the energy concentration of GIIRS.

Due to the impact of the noise in star images, the raw coordinate (X_i, Y_i) calculated above is not accurate enough. Thus, the information of the image sequence is efficiently used to improve the precision of the centroiding result by fitting the trajectory of the star centroid. Since the imaging moment of each frame is accurate by contrast, the trajectory is fitted in X and Y directions separately. According to the analysis in Section II-B, the star spot moves in a straight line in the image, thus the star trajectory can be linearly modeled as

$$\begin{cases} \hat{X}_i = \hat{a_x} t_i + \hat{b_x} \\ \hat{Y}_i = \hat{a_y} t_i + \hat{b_y} \end{cases} \quad (13)$$

where t_i is the imaging moment of the i-th star image, and $\hat{a_x}, \hat{b_x}, \hat{a_y}, \hat{b_y}$ are the coefficients of the trajectories in X and Y directions respectively, which can be optimally solved by least square fitting (LSF) via minimizing the fitting errors, i.e.

$$\begin{cases} \arg\min \left(\sum \frac{1}{2} (X_i - \hat{X}_i)^2 \right) \\ \arg\min \left(\sum \frac{1}{2} (Y_i - \hat{Y}_i)^2 \right) \end{cases} \quad (14)$$

The fitting results are shown in Figure 9. Putting the imaging moments into Equation 13, the revised coordinates in high precision of the star centroids in the image sequence can be obtained.

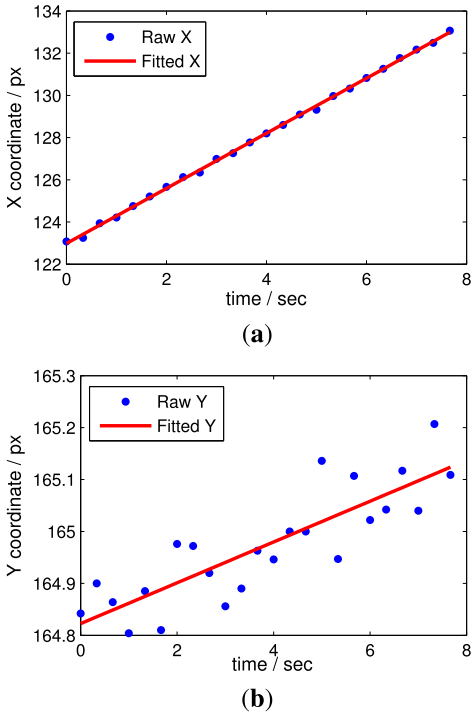

FIGURE 9. The results of the X (a) and Y (b) coordinates fitted by LSF.

IV. SIMULATION EXPERIMENTS

In order to evaluate the performance of our detection and centroiding method in different situations, a series of simulation experiments are designed in advance.

A. STAR IMAGE SIMULATION

As shown in Figure 10, $O_wX_wY_wZ_w$ represents the celestial coordinate system, in which the coordinate of star s is $\mathbf{X} = [cos\,\alpha\,cos\,\delta \quad sin\,\alpha\,cos\,\delta \quad sin\delta]^T$, where α and δ are the right ascension and the declination of s as defined above. $O_wX_cY_cZ_c$ is the Camera Coordinate System, which

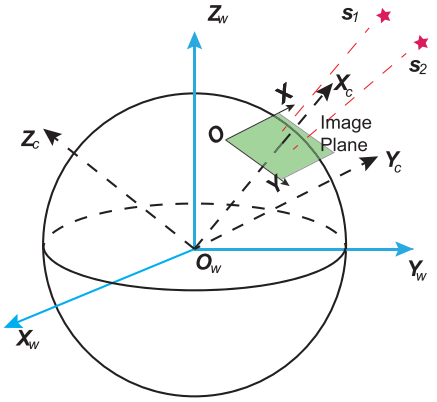

FIGURE 10. The coordinate systems used in the simulation.

is used to make the transition from $O_wX_wY_wZ_w$ to the Image Coordinate System OXY. The coordinate of star s in OXY can be calculated as

$$\mathbf{Y} = \mathbf{D}\mathbf{R_y}(-\delta_p)\mathbf{R_z}(\alpha_p)\mathbf{X} + \mathbf{Y_o} \tag{15}$$

where $\mathbf{Y} = [x \quad y]^T$ is the image coordinate, $\mathbf{Y_o} = [128 \quad 165]^T$ is the coordinate of the image center, and α_p and δ_p are the directional angles of line-of-sight (LOS) in $O_wX_wY_wZ_w$ system. $\mathbf{R_y}(\cdot)$ and $\mathbf{R_z}(\cdot)$ are the rotation matrices in Y and Z directions respectively as

$$\mathbf{R_y}(\theta) = \begin{bmatrix} cos\,\theta & 0 & -sin\,\theta \\ 0 & 1 & 0 \\ sin\,\theta & 0 & cos\,\theta \end{bmatrix} \tag{16}$$

$$\mathbf{R_z}(\theta) = \begin{bmatrix} cos\,\theta & sin\,\theta & 0 \\ -sin\,\theta & cos\,\theta & 0 \\ 0 & 0 & 1 \end{bmatrix} \tag{17}$$

$\mathbf{D}$ is the projection matrix which is used to switch to the image coordinate. Since the star is at infinity in $O_wX_cY_cZ_c$, $\mathbf{D}$ can be represented as

$$\mathbf{D} = \begin{bmatrix} 0 & -\frac{1}{\psi} & 0 \\ 0 & 0 & -\frac{1}{\psi} \end{bmatrix} \tag{18}$$

where ψ is the angular resolution of GIIRS as in Equation 2.

A star can be regarded as a point light source, since it is considered at infinity of imaging system. Thus, 2D Gaussian function is used as the point spread function (PSF) of GIIRS to simulate the energy distribution of the star spot in the image plane. Ideally, double integral of PSF in range of a pixel is used to calculate the gray value, modeling the photon accumulation.

In this simulation experiment, the mean image of an actual sequence without stars is used to model the fixed noise of our simulated images. Besides, zero-mean Gaussian white noise is added to the star image to simulate the random noise. To model the focal mode of GIIRS, the standard deviation of PSF (σ_{PSF}) is set to 0.3 pixels. The entire energy of a star with magnitude M is quantified as

$$\beta = \beta_0 \cdot 2.51^{-(M-M_0)} \tag{19}$$

where $\beta_0 = 100$ is the reference energy of the star with magnitude of $M_0 = 7.0$. To resemble the truth as possible, shading condition in the four corners of the image is considered, modeling the influence of the lens hood. The imaging frequency is set to 3 Hz, and each sequence consists of 24 frames of star images, the same as those of GIIRS in-orbit.

B. SIMULATED STAR IMAGE DATASET

Using the simulation procedure mentioned above, we simulate the following two subsets of star images for experimenting.

1) SINGLE STAR SUBSET

In this subset, only a single star is simulated in each image, with the initial Y coordinate from 165 to 165.99 with a step of 0.01 pixel. The standard deviation of noise (σ_n) is set from 0 to 10 with a step of 2. Meanwhile, the magnitude varies from 3.5 to 7.0 with a step of 0.5. Our detection and centroiding method is tested based on this subset. Figure 11, Figure 12 and Figure 13 show the star regions of the sample images with different simulation parameters.

2) CONSTELLATION SUBSET

In this subset, a constellation consisting of more than one star is generated in each image based on the real information of SAO star catalog, in order to test the performance of our star recognition method. A sample simulated image of the nine-star area mentioned in Section III-C is shown as Figure 14.

C. PERFORMANCE OF STAR DETECTION

We compare our star detection method with gray projecting integral (GPI) [14], [15], a classical method for target detection. Experiments are performed after fixed noise removal. Table 3 shows the star detection results under different noise levels where the magnitude of the star is set to 6.5, and Table 4 shows the results under different magnitudes where σ_n is set to 6.

According to Table 3, it is clear that noise in the star images does harm to the precision of GPI method. By contrast, our detection method has better robustness against noise. In addition, the recall rate of ours is higher than GPI, reaching 99.87% ($\sigma_n = 10$). This is because our detection method takes full advantage of the movement information, making a distinction between star spots and noisy pixels. From Table 4, it can be seen that our detection method performs well to all magnitudes, guaranteeing 83% precision and 100% recall rate. The precision of our star detection method is obviously better than GPI, especially when the magnitude becomes higher, i.e. the star becomes darker.

D. PERFORMANCE OF STAR RECOGNITION

Our star recognition method is tested to all of the 4423 constellations in the FOV of GIIRS, with the star number (N_s) from 2 to 9. The experimental results are shown in Figure 5.

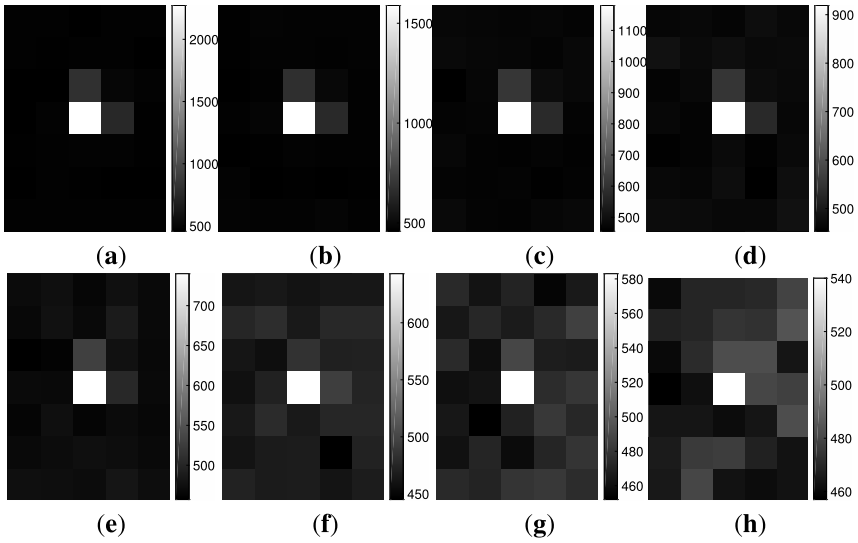

FIGURE 11. Star regions of simulated star images with the magnitude of (a) 3.5, (b) 4.0, (c) 4.5, (d) 5.0, (e) 5.5, (f) 6.0, (g) 6.5, and (h) 7.0.

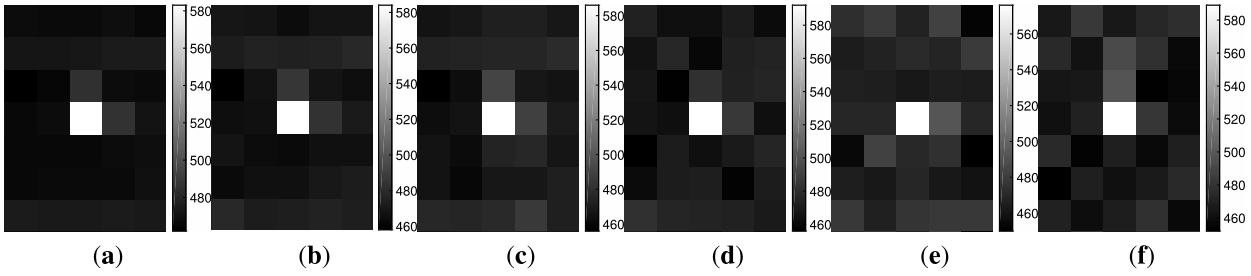

FIGURE 12. Star regions of simulated star images in different noise level, with σ_n of (a) 0, (b) 2, (c) 4, (d) 6, (e) 8 and (f) 10.

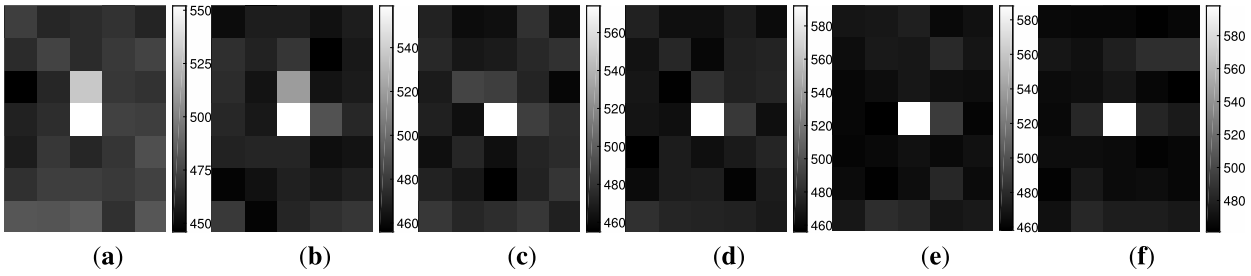

FIGURE 13. Star regions of simulated star images with the initial Y coordinate of (a) 0.00, (b) 0.10, (c) 0.20, (d) 0.30, (e) 0.40, and (f) 0.50. Considering the symmetry of 2D Gaussian PSF, those with the initial Y coordinates from 0.60 to 0.90 are omitted.

TABLE 3. Precision (ϵ_p) and recall (ϵ_r) for star detection under different noise levels.

Method	Indicator	σ_n =0	σ_n =2	σ_n =4	σ_n =6	σ_n =8	σ_n =10
GPI	ϵ_p	100.00%	87.17%	63.32%	67.29%	68.95%	68.39%
	ϵ_r	100.00%	100.00%	100.00%	100.00%	99.90%	98.92%
Ours	ϵ_p	100.00%	87.84%	85.74%	86.20%	85.65%	85.64%
	ϵ_r	100.00%	100.00%	100.00%	100.00%	99.99%	99.87%

It can be seen that our recognition method performs well with different star numbers, achieving the success rate better than 93.75%. Owing to our improvement to the triangular algorithm, over 95.8% of the images with two stars can be correctly recognized.

E. PERFORMANCE OF CENTROID EXTRACTION

We perform comparison with the popular centroid extraction method COM [7] under different noise levels and star magnitudes to quantitatively evaluate the precision of our centroiding method. Results are shown in Table 6 and Table 7.

TABLE 4. Precision (ϵ_p) and recall (ϵ_r) for star detection under different magnitudes.

Method	Indicator	mag =3.5	mag =4.0	mag =4.5	mag =5.0	mag =5.5	mag =6.0	mag =6.5	mag =7.0
GPI	ϵ_p	100.00%	100.00%	100.00%	96.46%	79.47%	66.67%	67.99%	64.34%
	ϵ_r	100.00%	100.00%	100.00%	100.00%	100.00%	100.00%	100.00%	100.00%
Ours	ϵ_p	100.00%	100.00%	100.00%	100.00%	100.00%	83.33%	89.89%	91.60%
	ϵ_r	100.00%	100.00%	100.00%	100.00%	100.00%	100.00%	100.00%	100.00%

TABLE 5. Performance of star recognition.

Star number	$N_s = 2$	$N_s = 3$	$N_s = 4$	$N_s = 5$	$N_s = 6$	$N_s = 7$	$N_s = 8$	$N_s = 9$
Execution times	30597	7056	1320	264	216	240	96	24
Succeeding times	29312	6732	1253	255	205	229	90	24
Success rate	95.80%	95.41%	94.92%	96.59%	94.91%	95.42%	93.75%	100.00%

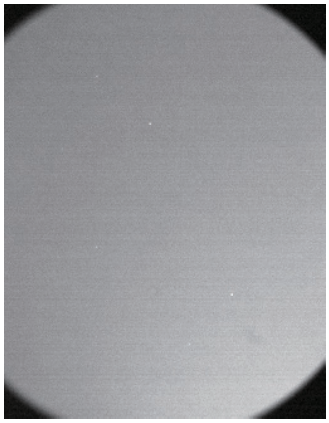

FIGURE 14. Simulated GIIRS star image in constellation subset. The LOS of the IFOV of the simulated star image is *rightascension* = 84.063°, *declination* = −5.648°. There are nine stars with the magnitude under 7.0 in this frame.

TABLE 6. Centroiding error under different noise levels. ε_x and ε_y are the errors in X and Y direction respectively. The integrate centroiding error ε_o is the Euclid distance between extracted centers and ground truth in image plane.

		σ_n =0	σ_n =2	σ_n =4	σ_n =6	σ_n =8	σ_n =10
COM	ε_x	0.0820	0.0786	0.0807	0.0897	0.1029	0.1188
	ε_y	0.0325	0.0440	0.0714	0.0988	0.1266	0.1573
	ε_o	0.0929	0.0973	0.1189	0.1473	0.1796	0.2165
Ours	ε_x	0.0171	0.0298	0.0417	0.0558	0.0680	0.0785
	ε_y	0.0323	0.0361	0.0561	0.0786	0.1010	0.1265
	ε_o	0.0389	0.0519	0.0765	0.1043	0.1305	0.1594

As shown in Table 6, it is clear that the precision of our centroiding method is higher than that of COM, especially for the X coordinate. It is because the centroid of the star moves slightly in X direction due to the geostationary orbit of FY-4A. Thus, our centroiding method based on trajectory fitting has a higher precision in X direction than Y. The actual centroiding error of ours is less than 0.1594 pixels even under the strongest noise ($\sigma_n = 10$). Table 7 indicates that our centroiding method works well in different magnitudes. The centroiding error is less when the star is brighter (lower magnitude), since the energy distribution is reserved better relatively with the same noise level.

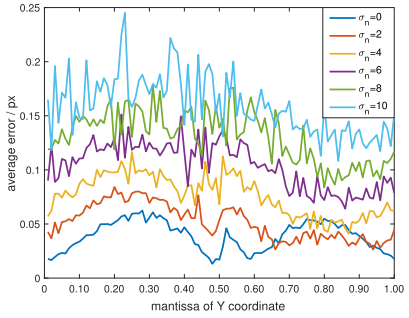

FIGURE 15. Centroiding error of our method under different mantissa of initial Y coordinate with σ_n from 0 to 10.

It should be noticed that initial Y coordinate of star centroid is also an important factor in the energy distribution of the star spot. More energy is distributed in a pixel when the mantissa of Y is close to 0.5, and most of the energy is distributed into two pixels in Y direction when that is 0.0. Figure 15 shows the centroiding error of our method under different mantissa of initial Y coordinate with various noise (σ_n from 0 to 10). It indicates that the initial Y coordinate of the trajectory has influence on the precision, especially for the star images with tiny noise. Best centroiding results are obtained around the mantissa of Y=0.5. The noise is another important factor affecting the centroiding precision.

V. IN-ORBIT TESTING RESULTS

Our proposed method has been tested for over 2 years in actual in-orbit tasks, since the launch of FY-4A on December 11, 2016. The results of the in-orbit test verify the effectiveness and good precision of our method for star centroid extraction of GIIRS. We show some of the in-orbit testing results in this section.

A. EFFECTIVENESS OF STAR CENTROIDING

Table 8 shows the execution success ratio (definition in [11]) of our method during the in-orbit test from 2017/04/12 to 2017/04/17, which is calculated with totally 23078 times of GIIRS centroiding in this period. It can be seen that our method performs well in non-midnight with the execution success ratio over 98%, except the three hours around local

TABLE 7. Centroiding error of our method under different magnitudes. ε_x and ε_y are the errors in X and Y direction respectively. The integrate centroiding error ε_o is the Euclid distance between extracted centers and ground truth.

		mag =3.5	mag =4.0	mag =4.5	mag =5.0	mag =5.5	mag =6.0	mag =6.5	mag =7.0
COM	ε_x	0.0817	0.0810	0.0812	0.0796	0.0781	0.0811	0.0830	0.1159
	ε_y	0.0529	0.0549	0.0577	0.0605	0.0686	0.0806	0.1015	0.1884
	ε_o	0.1022	0.1029	0.1050	0.1059	0.1114	0.1240	0.1444	0.2406
Ours	ε_x	0.0155	0.0178	0.0255	0.0258	0.0313	0.0391	0.0588	0.0852
	ε_y	0.0529	0.0546	0.0572	0.0598	0.0670	0.0777	0.0900	0.1740
	ε_o	0.0560	0.0587	0.0657	0.0682	0.0771	0.0914	0.1107	0.2041

TABLE 8. The execution success ratio of our method.

Date	Non-midnight	Midnight (Local time 22:30-01:30)
2017/04/12	98.25%	75.78%
2017/04/13	98.70%	78.62%
2017/04/14	98.67%	79.27%
2017/04/15	98.56%	78.40%
2017/04/16	98.72%	73.91%
2017/04/17	98.14%	66.67%

time 0 o'clock (22:30-01:30). In midnight, the success ratio reduces to the worst 66.67%. This is because the sun is close to the LOS of GIIRS on account of the geostationary orbit of FY-4A, causing a lot of stray light passing into the imaging device. The star images suffer from saturation and low SNR, leading to the failure of some star sensing tasks.

TABLE 9. Centroiding error of our method in actual observation data of GIIRS.

Error/px	Times	Percentage	Subtotal
0.00-0.05	133	12.21%	12.21%
0.05-0.10	253	23.23%	35.44%
0.10-0.15	244	22.41%	57.85%
0.15-0.20	167	15.34%	73.19%
0.20-0.25	116	10.65%	83.84%
0.25-0.30	74	6.80%	90.64%
$\geq$0.30	102	9.37%	100.00%
Total	1089	100%	–

B. PRECISION OF STAR CENTROIDING

Due to the lack of ground truth centroid coordinates during the in-orbit test, we quantitatively evaluate the precision of our centroiding method by two ways. In one way, the star centroids of the actual images are labeled visually as the ground truth. In the other way, the star angular distance between two sensed stars (Equation 10) can be calculated to compare with their angular distance in the star catalog (Equation 11). The actual star images captured by GIIRS in-orbit on July 25, 2017, total 1089 sequences, are used for visual comparison resutls in Table 9, and total 1256 sequences which contain more than two stars from 2017/04/12 to 2017/04/17 are used to evaluate the centroiding precision shown in Table 10.

As shown in Table 9, the error of over 90% centroiding results is less than 0.3 pixels based on visual evaluation. Over 73% results are more precise with error less than 0.2 pixels. Table 10 shows that the average star angular distance error is

TABLE 10. Angular distance error of our method in actual observation data of GIIRS.

Date	2 stars	3 stars	Average angular distance error
2017/04/12	233	5	0.266
2017/04/13	209	5	0.281
2017/04/14	235	2	0.261
2017/04/15	213	3	0.277
2017/04/16	207	3	0.265
2017/04/17	159	0	0.265
Total	1256	18	0.269

0.269 pixels. It can be concluded that our method performs well on in-orbit star images, achieving high centroiding precision with centroiding error less than 0.3 pixels.

VI. CONCLUSIONS

In this paper, a star detection and centroiding method for GIIRS aboard FY-4A has been proposed, containing the complete star image processing of noise removal, star detection, star recognition, and centroid extraction. The weak point target detection task is translated into a trajectory detection, which significantly improves the star detection precision and recall rate to 85.64% and 99.87% for the images with the standard deviation of noise $\sigma_n = 10$. Besides, the centroiding error is reduced to 0.1594 pixels in the simulated images ($\sigma_n = 10$), through the trajectory fitting process in our centroiding method. Over-2-year in-orbit tests have proved the effectiveness and precision of our star detection and centroiding method for GIIRS, laying the foundation for the high-precision image navigation for GIIRS of FY-4A.

REFERENCES

[1] J. Yang, Z. Zhang, C. Wei, F. Lu, and Q. Guo, "Introducing the new generation of chinese geostationary weather satellites, Fengyun-4," *Bull. Amer. Meteorol. Soc.*, vol. 98, no. 8, pp. 1637–1658, Aug. 2017.

[2] S. I. Rani, D. Srinivas, and J. P. George, "A review of the space based remote sensing for NWP," *Proc. SPIE*, vol. 9876, May 2016, Art. no. 98762H.

[3] J. Yang, "Development and applications of China's Fengyun (FY) meteorological satellite," *Spacecraft Eng.*, vol. 17, no. 3, pp. 23–28, May 2008.

[4] F. Lu and Y. Shou, "Channel simulation for FY-4 AGRI," in *Proc. Geosci. Remote Sens. Symp.*, Jul. 2011, pp. 3265–3268.

[5] W. Lyu, T. Wang, Y. Dong, and Y. Shen, "Imaging navigation and registration for geostationary imager," *IEEE Geosci. Remote Sens. Lett.*, vol. 14, no. 12, pp. 2175–2179, Dec. 2017.

[6] L. I. Xiao-Kun, G.-Q. Wang, and G.-L. Chen, "FY-4 imager: Visible channel star sensing," *Sci. Technol. Eng.*, vol. 7, no. 6, pp. 993–996, 2007.

[7] C. C. Liebe, "Accuracy performance of star trackers—A tutorial," *IEEE Trans. Aerosp. Electron. Syst.*, vol. 38, no. 2, pp. 587–599, Apr. 2002.

[8] J. Yang, B. Liang, T. Zhang, and J. Song, "A novel systematic error compensation algorithm based on least squares support vector regression for star sensor image centroid estimation," *Sensors*, vol. 11, no. 8, pp. 7341–7363, 2011.

[9] X. Wang, X. Wei, Q. Fan, J. Li, and G. Wang, "Hardware implementation of fast and robust star centroid extraction with low resource cost," *IEEE Sensors J.*, vol. 15, no. 9, pp. 4857–4865, Sep. 2015.
[10] T. Kampe, "SIRAS-G, the spaceborne infrared atmospheric sounder: Infrared imaging spectroscopy from geosynchronous orbit," in *Proc. AIAA Space Conf.*, 2003, p. 6250.
[11] H. Zhang *et al.*, "Accurate star centroid detection for the advanced geosynchronous radiation imager of Fengyun-4a," *IEEE Access*, vol. 6, no. 1, pp. 7987–7999, Mar. 2018.
[12] G.-J. Zhang, X.-G. Wei, and J. Jiang, "Star map identification based on a modified triangle algorithm," *Acta Aeronautica Astron. Sinca*, vol. 27, no. 6, pp. 1150–1154, Nov. 2006.
[13] M. S. Arani, A. Toloei, and Z. Eghbaleh, "A geometric star identification algorithm based on triple triangle pattern," in *Proc. 7th Int. Conf. Recent Adv. Space Technol. (RAST)*, Jun. 2015, pp. 81–85.
[14] W. Zhang, Q. Chen, D. Du, and Z. Sun, "Gray projecting integral method for line detection," *J. Tsinghua Univ. (Sci. Technol.)*, vol. 45, no. 11, pp. 1446–1449, 2005.
[15] L.-H. Ren, K. Liu, H.-Y. Zhang, and H. Yang, "Rectangle detection of gray projection integral extreme value method," *Comput. Eng.*, vol. 38, no. 8, pp. 159–160, 2012.

HAOPENG ZHANG received the B.S. and Ph.D. degrees from Beihang University, Beijing, China, in 2008 and 2014, respectively, where he is currently an Assistant Professor with the Image Processing Center, School of Astronautics. His main research interests include remote sensing image processing, multi-view object recognition, 3-D object recognition and pose estimation, and other related areas in pattern recognition, computer vision, and machine learning. He is a member of the IEEE.

YI SU received the B.S. degree from Beihang University, Beijing, China, in 2016, where he is currently pursuing the master's degree with the Image Processing Center, School of Astronautics. His research interests include computer vision and pattern recognition.

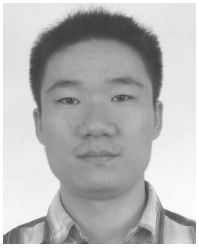

LEI YANG received the B.S. and M.S. degrees in applied mathematics from Northeastern University, China, in 2000 and 2003, respectively, and the Ph.D. degree in pattern recognition and intelligent systems from the Institute of Automation, Chinese Academy of Sciences, in 2006. He is currently a Professor with the National Satellite Meteorological Center, China Meteorological Administration. His current research interests include system design and implementation on image navigation and registration for China Fengyun meteorological satellites.

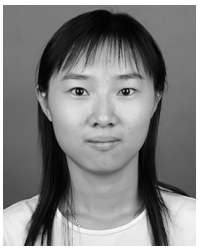

JIAN SHANG received the Ph.D. degree in communication and information system from the Institute of Electronics, Chinese Academy of Sciences, Beijing, China, in 2009. She is currently with the National Satellite Meteorological Center, China Meteorological Administration. Her research interests include remote sensing information processing and remote sensing instrument design.

CHENGBAO LIU received the Ph.D. degree from the University of Chinese Academy of Sciences, in 2013. He is currently with the National Satellite Meteorological Center, China Meteorological Administration. His main research interest is the geolocation algorithm for the remote sensing data of Chinese meteorological satellites.

JING WANG received the Ph.D. degree in optical engineering from the Beijing Institute of Technology, in 2015. She is currently with the National Satellite Meteorological Center, China Meteorological Administration. Her current research interest includes implementation on image navigation for China meteorological satellites.

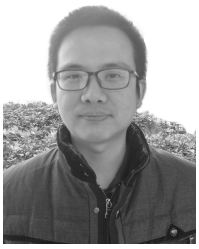

SHENGXIONG ZHOU received the B.S. degree from Wuhan University, Wuhan, China, in 2004. He is currently with the Southwest Electronics and Telecommunication Technology Research Institute. His research interests include image positioning, data processing, and system architecture design.

ZHIGUO JIANG received the B.S., M.S., and Ph.D. degrees from Beihang University, Beijing, China, in 1987, 1990, and 2005, respectively, where he is currently a Professor with the School of Astronautics. His current research interests include remote sensing image analysis, target detection, tracking and recognition, and medical image processing. He currently serves as a standing member of the Executive Council of the China Society of Image and Graphics and also as a member of the Executive Council of the Chinese Society of Astronautics. He is an Editor of the *Chinese Journal of Stereology and Image Analysis*.

ZHIQING ZHANG received the B.S. degree in radio engineering from Northeastern University, China, in 1986. He is currently a Senior Professor of engineering and the Chief Designer with the National Satellite Meteorological Center, China Meteorological Administration, China. His current research interests include system design and implementation on ground segment and application systems for China geostationary meteorological satellite.